Atomic-Scale Magnetism of Cr-Doped Bi_2Se_3 Thin Film Topological Insulators

Wenqing Liu,[†,‡,▽] Damien West,[§,▽] Liang He,[†,∥,▽] Yongbing Xu,[*,†,‡] Jun Liu,[⊥] Kejie Wang,[†] Yong Wang,[⊥] Gerrit van der Laan,[#] Rong Zhang,[*,†] Shengbai Zhang,[*,§] and Kang. L. Wang[*,∥]

[†]York-Nanjing Joint Center (YNJC) for Spintronics and Nanoengineering, School of Electronics Science and Engineering, Nanjing University, Nanjing 210093, China, [‡]Spintronics and Nanodevice Laboratory, Department of Electronics, University of York, York YO10 5DD, United Kingdom, [§]Department of Physics, Applied Physics, and Astronomy, Rensselaer Polytechnic Institute, Troy, New York 12180, United States, [∥]Department of Electrical Engineering, University of California, Los Angeles, Los Angeles, California 90095, United States, [⊥]Center of Electron Microscopy, State Key Laboratory of Silicon Materials, Department of Materials Science and Engineering, Zhejiang University, Hangzhou 310027, China, and [#]Magnetic Spectroscopy Group, Diamond Light Source, Didcot OX11 0DE, United Kingdom. [▽]W.L., D.W., and L.H. contributed equally to this work.

ABSTRACT Magnetic doping is the most common method for breaking time-reversal-symmetry surface states of topological insulators (TIs) to realize novel physical phenomena and to create beneficial technological applications. Here we present a study of the magnetic coupling of a prototype magnetic TI, that is, Cr-doped Bi_2Se_3, in its ultrathin limit which is expected to give rise to quantum anomalous Hall (QAH) effect. The high quality $Bi_{2-x}Cr_xSe_3$ epitaxial thin film was prepared using molecular beam epitaxy (MBE), characterized with scanning transimission electron microscopy (STEM), electrical magnetotransport, and X-ray magnetic circularly dichroism (XMCD) techniques, and the results were simulated using density functional theory (DFT) with spin−orbit coupling (SOC). We observed a sizable spin moment $m_{spin} = (2.05 \pm 0.20)\ \mu_B$/Cr and a small and negative orbital moment $m_{orb} = (-0.05 \pm 0.02)\ \mu_B$/Cr of the $Bi_{1.94}Cr_{0.06}Se_3$ thin film at 2.5 K. A remarkable fraction of the $(Cr_{Bi}-Cr_I)^{3+}$ antiferromagnetic dimer in the $Bi_{2-x}Cr_xSe_3$ for $0.02 < x < 0.40$ was obtained using *first-principles* simulations, which was neglected in previous studies. The spontaneous coexistence of ferro- and antiferromagnetic Cr defects in $Bi_{2-x}Cr_xSe_3$ explains our experimental observations and those based on conventional magnetometry which universally report magnetic moments significantly lower than 3 μ_B/Cr predicted by Hund's rule.

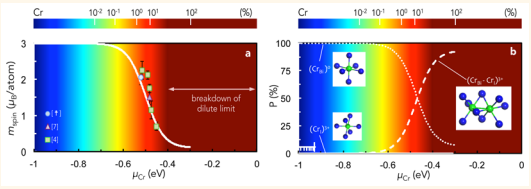

KEYWORDS: magnetic topological insulator · spin and orbital moments · XMCD · density functional theory · spintronics

Three-dimensional topological insulators (TIs) represent unusual phases of quantum matter with an insulating bulk gap and gapless Dirac-like band dispersion surface states. Unlike the different electronic properties of the surface and the bulk universally existing in all solids owing to the inevitable termination of the periodic lattice structure near the surface, TIs present a new class of nontrivial surface states arising from the intrinsic strong SOC. These robust low-dimensional conducting states are topologically protected against time-reversal-invariant perturbations, such as scattering by nonmagnetic impurities, crystalline defects, and surface distortions. While such a phase offers unique opportunities for fundamental research, it is equally important to break the time-reversal symmetry of TIs to realize novel physical phenomena and quantum-computing applications. The newly demonstrated QAH effect,[1−3] abnormal proximity effect,[4,5] giant magneto-optical Kerr effect,[6] magnetic monopole,[7] and chiral conduction channels[8,9] are some of the fascinating examples. Within the growing family of TIs, ferromagnetism has been reported in V-, Cr-, and Mn-doped single crystals of Sb_2Te_3,[10,11] Fe- and Mn-doped single crystals of Bi_2Te_3,[12,13] and Mn-doped single crystals of Bi_2Se_3.[14] Both ferro-[15] and antiferromagnetism[16] have been reported in Cr-doped Bi_2Se_3, and for Fe-doped Bi_2Se_3 observations are rather controversial. Zhang et al.[17] studied the effect of magnetic doping of a series of 3*d* transition metals in Bi_2Se_3 using *first-principles* calculations and found that Cr and Fe doping preserves the insulating nature of the host TI in the bulk and Cr-doped Bi_2Se_3 is likely to be ferromagnetic. Apart from transition metals, rare-earth metals such as Gd,[18] Dy, and Sm[19] have also been explored as an effective dopant to induce long-range magnetic ordering in Bi_2Se_3[20] or Bi_2Te_3.

* Address correspondence to yongbing.xu@york.ac.uk, rzhang@nju.edu.cn, zhangs9@rpi.edu, wang@seas.ucla.edu.

Received for review June 29, 2015 and accepted September 8, 2015.

Published online September 08, 2015
10.1021/acsnano.5b03980

TABLE 1. Reported Experimental Values for the Magnetic Moment of Magnetically Doped Bi_2Se_3

system	method	m_{total} (μ_B/atom)	ref
$Bi_{1.94}Cr_{0.06}Se_3$	XMCD	2.00 ± 0.20	this work
$Bi_{1.98}Cr_{0.02}Se_3$	SQUID-VSM	0.4	18
$Bi_{1.76}Cr_{0.24}Se_3$	neutron scattering	1.5	24
$Bi_{1.90}Cr_{0.1}Se_3$	SQUID-VSM	2.0	15
$Bi_{1.77}Cr_{0.23}Se_3$	XMCD	2.9 ± 0.3	21
$Bi_{1.98}Mn_{0.02}Se_3$	SQUID-VSM	1.5	14
$Bi_{1.995}Fe_{0.005}Se_3$	SQUID-VSM	3.2	14
$Bi_{1.98}Gd_{0.02}Se_3$	SQUID-VSM	6.9 ± 0.2	18

For the electronic and magnetic ground state of the magnetically doped TIs, evidence from the experimental observations including magneto-transport measurements,[49,50] global magnetometry,[14,15,49] and core-level spectroscopies[21−23] are so far inconclusive. Magnetic studies on epitaxial, Cr-doped Bi_2Se_3 using superconducting quantum interference device-vibrating sample magnetometer magnetometry (SQUID-VSM)[15] and polarized neutron reflectometry (PNR)[24] universally reported a magnetic moment of no more than ~2 μ_B/atom, remarkably lower than the Hund's rule of 3 μ_B/atom of substitutional Cr^{3+} on Bi sites. Significant mismatch also exists in Mn- and Fe-doped Bi_2Se_3, who typically show global magnetic moments of ~1.5 and ~3 μ_B/atom,[14] while their Hund's rule is 5 μ_B/atom. Table 1 gathers the magnetic moment of Bi_2Se_3 for various magnetic dopants. It has been proposed that in magnetic TIs, ferromagnetic moments can be developed not only through the *s-d* exchange interaction such as in diluted magnetic semiconductors (DMSs),[25−29] but also through the van Vleck mechanism, by which magnetic ions are directly coupled through the local valence elecrons.[3] Both types of mechanism have been observed independently in Mn-doped $Bi_2(TeSe)_3$[30] and Cr-doped $(BiSb)_2Te_3$[31] thin films. Given the fact that the magnetic state of a doped TI can be independent of the carrier concentration, it is timely and important to obtain an insight of the detailed chemical bonds of the magnetic impurities. In this regard, the synchrotron-based techniques of XMCD are ideal valence-, site-, and symmetry-specific probes.[32,23,33−37] In this paper, we present a comprehensive study of magnetism of a prototypical magnetic TI, i.e., $Bi_{2-x}Cr_xSe_3$, in its ultrathin limit which is expected to give rise to QAH effect.[3] According to the pioneering work by Haazen et al.,[15] the magnetic moment of $Bi_{2-x}Cr_xSe_3$ decreases with increasing doping concentration and sharply drops beyond ~10%. On the other hand, excessively low Cr concentrations, that is, <1%, form no long-range magnetic ordering.[49] Therefore, we selected a 3% Cr-doped Bi_2Se_3 or $Bi_{1.94}Cr_{0.06}Se_3$ thin film to perform the detailed XMCD study. Using XAS and XMCD, we quantitatively addressed the magnetic moments of the epitaxial $Bi_{1.94}Cr_{0.06}Se_3$ thin film, and the results were compared with *first-principle* calculations to get an insight of the nature of the magnetic coupling.

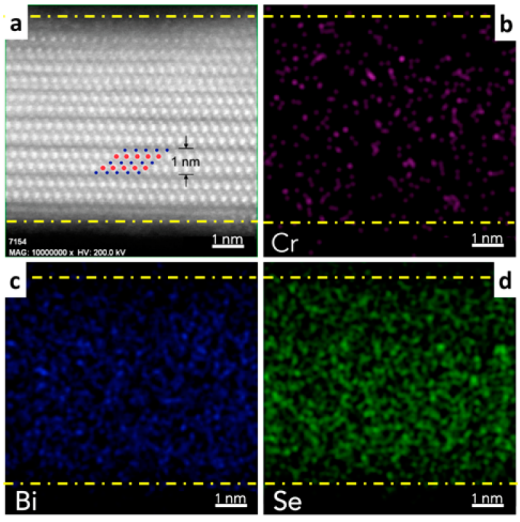

Figure 1. STEM characterization. (a) Typical HAADF image showing the highly ordered hexagonal and quintuple layer structure of the prepared $Bi_{2-x}Cr_xSe_3$/Si(111) thin film samples. The red and blue dots represent the Bi and Se columns, respectively, within one quintuple layer. The dash-dotted lines indicate the boundaries of the $Bi_{2-x}Cr_xSe_3$ thin film with the Al_2O_3 cap and the Si substrate, respectively. (b−d) EDX color maps of (b) Cr, (c) Bi, and (d) Se.

RESULTS AND DISCUSSION

The 10 nm $Bi_{1.94}Cr_{0.06}Se_3$/Si(111) thin films used in this study was prepared using MBE. First the crystalline structure of the prepared samples was characterized using high-angle annular dark-field (HAADF) high-resolution STEM. Cross-sectional foils of $Bi_{1.94}Cr_{0.06}Se_3$/Si(111) were prepared by focused ion beam (FIB), during which all parameters were carefully optimized to avoid ion injection and specimen damage, including the accelerating voltage, beam current, and tilt angle.[4] Figure 1a presents a typical HAADF image of the $Bi_{1.94}Cr_{0.06}Se_3$/Si(111), in which the Bi and Se columns (marked by red and blue solid circles, respectively) can be clearly identified owing to the *Z*-contrast sensitivity of the HAADF imaging technique. The dark regions outside $Bi_{1.94}Cr_{0.06}Se_3$ corresponds to the Al_2O_3 cap and Si substrate, respectively, which cannot be demonstrated using the present mode since they are composed of much lighter atoms than Bi and Se. The Cr dopants are uniformly distributed within the Bi_2Se_3 film, as can be seen from the EDX color maps of the Cr, Bi, and Se, respectively, in Figure 1b−d. Overall, the HAADF images confirm the highly ordered hexagonal and quintuple-layered structure of the prepared $Bi_{1.94}Cr_{0.06}Se_3$/Si(111) thin films without appreciable Cr segregations or secondary phases.[38,39] It should be noted that even though these images solely are not sufficient to evidence the entry modes of the Cr dopants in the Bi_2Se_3 matrix for the similar reason as the inaccessibility of the Al atoms.

The global magnetic response of the epitaxial $Bi_{1.96}Cr_{0.06}Se_3$/Si(111) thin film samples was examined by magneto-transport measurements by patterning

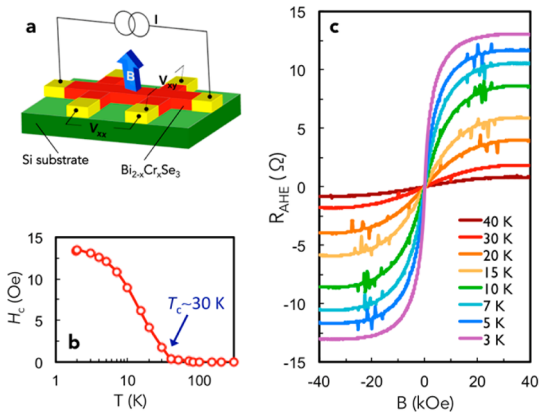

Figure 2. Electrical magneto-transport measurements. (a) Schematic diagram of the experimental setup of the QAH effect measurement. (b) H_c versus temperature of the $Bi_{1.94}Cr_{0.06}Se_3$/Si(111) thin film from 3 to 300 K. (c) R_{AHE} versus magnetic field B of the thin film from 3 to 40 K after background removal.

into standard Hall bar devices, using conventional optical photolithography and a subsequent CHF_3 dry etching for 20 s. As shown in Figure 2a, six Hall channel contacts (10 nm Ti and 100 nm Au) were defined by e-beam evaporation. Standard four-terminal electrodes were fabricated to eliminate the contact resistance. A constant AC current of 0.05−0.1 μA with a frequency of 1.3 kHz is fed through two outer contacts, and the voltage drop across the inner pads is measured to determine the resistance. By subtracting the ordinary Hall component, we plotted the anomalous Hall resistance ($R_{AHE} = R_{xy} \sim R_0H$)[40] as a function of the field applied perpendicularly to the film in Figure 2c, in which a nonzero R_{AHE} was observable up to ~30 K. Figure 2b presents the temperature dependence of the coercive field (H_c) estimated from the shift of the weak antilocalization (WAL) cusp under the opposite field scanning directions.[4,49] The H_c exhibits Curie-like behavior against the temperature and $T_c \approx 30$ K, consistent with that estimated from R_{AHE}.

X-ray absorption spectroscopy (XAS) measurements at the Cr $L_{2,3}$ absorption edge of the $Bi_{1.96}Cr_{0.06}Se_3$/Si(111) thin film were performed on beamline I10 at the Diamond Light Source, U.K. Circularly polarized X-rays with ~100% degree of polarization[41] were used in normal incidence with respect to the sample plane and parallel to the applied magnetic field, as illustrated in Figure 3a. The XMCD was obtained by taking the difference of the XAS spectra, that is, $\sigma^- - \sigma^+$, by flipping the X-ray helicity at a fixed magnetic field of 30 kOe, under which the sample is fully magnetized with negligible paramagnetic contribution.[4,49,50] Figure 3b presents a typical pair of XAS and XMCD spectra of the $Bi_{1.96}Cr_{0.06}Se_3$/Si(111) epitaxial thin film obtained at 2.5 K using total electron yield detection (TEY). The XAS of Cr shows multiple structures for both spin−orbit split core levels, suggesting a mixture of Cr with more than one valence state. This mixture can be analyzed

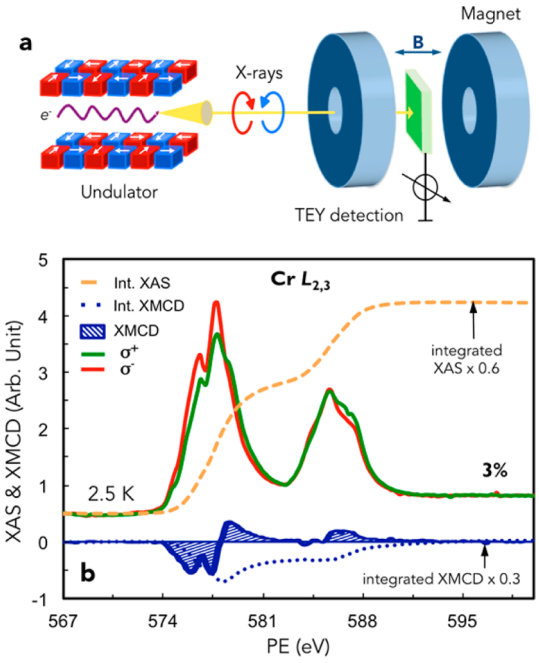

Figure 3. XAS/XMCD measurements. (a) Schematic diagram of the experimental setup for XAS and XMCD at the beamline, where the beamline optics has been omitted. (b) Typical pair of XAS and XMCD spectra of the $Bi_{1.94}Cr_{0.06}Se_3$/Si(111) thin film. Data are offset and scaled for clarity.

using atomic multiplet simulation of the spectrum as detailed in the Supporting Information, which indicates that the Cr dopants are primarily near-trivalent and the presence of a small amount of divalent Cr is most likely from the terminated surface of the $Bi_{2-x}Cr_xSe_3$ lattice.[21,22]

The spin (m_{spin}) and orbital (m_{orb}) magnetic moment of the $Bi_{1.96}Cr_{0.06}Se_3$/Si(111) thin film were obtained by applying the sum rules[42,43] to the integrated XMCD and summed XAS spectra of the Cr $L_{2,3}$ edges, based on

$$m_l = -\frac{4}{3} n_h \frac{\int_{L_{2,3}} (\sigma^- - \sigma^+) dE}{\int_{L_{2,3}} (\sigma^- + \sigma^+) dE}$$

$$m_s = -n_h \frac{6\int_{L_3} (\sigma^- - \sigma^+) dE - 4\int_{L_{2,3}} (\sigma^- - \sigma^+) dE}{\int_{L_{2,3}} (\sigma^- + \sigma^+) dE} \times SC - \langle T_z \rangle \quad (1)$$

where E, n_h, SC, and $\langle T_z \rangle$, represent the photon energy, number of d holes, spin correction (SC) factor, and magnetic dipole term, respectively. In order to exclude the nonmagnetic contribution of the XAS spectra an arctangent-based step function is used to fit the threshold.[44,45] The spectral overlap or j−j mixing[42] has to be taken into account because of the relatively small spin−orbit splitting in the Cr 2p level. The value of SC, that is, 2.0 ± 0.2 for Cr, was determined by calculating the $L_{2,3}$ multiplet structure for a given ground state, applying the sum rule on the calculated XMCD spectrum, and comparing the result with the

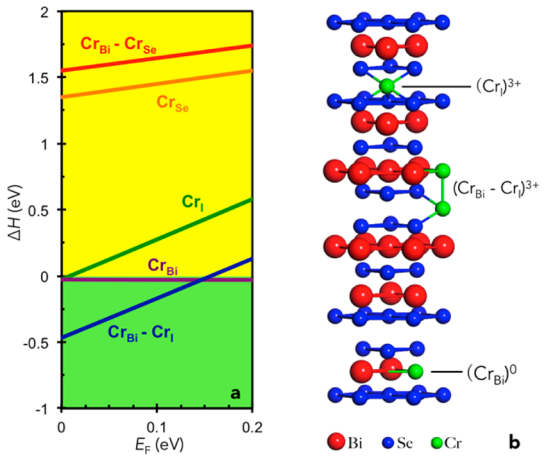

Figure 4. Cr-related defects in $Bi_{2-x}Cr_xSe_3$. (a) Formation energy ΔH of the Cr-related defects in $Bi_{2-x}Cr_xSe_3$ obtained under the given growth conditions as described in the text. The slopes indicate the stable charge states of the defect, and the zero of E_F corresponds to the valence band maximum (VBM). (b) Illustration of the three types of predominant defects in $Bi_{2-x}Cr_xSe_3$, *i.e.*, Cr_{Bi}^0, Cr_I^{3+}, and $(Cr_{Bi}-Cr_I)^{3+}$.

spin moment calculated directly for this ground state.[5,46] Assuming $n_h = 7$ on the majority trivalent Cr basis (see the Supporting Information), we obtained $m_{spin} = (2.05 \pm 0.20)\ \mu_B$/atom and $m_{orb} = (-0.05 \pm 0.02)$ for the $Bi_{1.94}Cr_{0.06}Se_3$/Si(111) thin film. That gives a total moment (m_{total}) of $(2.00 \pm 0.20)\ \mu_B$/atom as included in Table 1. The m_{orb} and m_{spin} have opposite signs, corresponding to an antiparallel alignment of spin and orbital moments in Cr. This agrees with the Hund's rule for Cr where the 3*d* shell is less than half full. The octahedral crystal-field interaction quenches m_{orb}, because the 3*d* electrons occupy the 3-fold degenerate majority-spin t_{2g} orbitals, leading to a nearly vanishing m_{orb} as observed here. For similar reasons the $\langle T_z \rangle$ is small and is not taken out from the m_{spin}, giving an error <5%.

We address the origin of the observed m_{spin} and m_{orb} of the $Bi_{1.94}Cr_{0.06}Se_3$/Si(111) thin film to this end. The layered structure of Bi_2Se_3 allows the Cr dopants not only to enter the host substitutionally, but also interstitially in the van der Waals gap between the layers. To investigate the m_{spin} and m_{orb} of Cr in Bi_2Se_3, it must first be determined where the Cr prefers to reside within the lattice. Although several prior works[17] have reported that substitutional Cr is energetically more favorable over interstitial Cr, if one considers only single impurities, these calculations leave out the possibility of the presence of complex defects. We calculated the formation energies (ΔH) of Cr at various lattice positions including not only the interstitial (denoted as Cr_I) and substitutional sites with Cr replacing Bi (denoted as Cr_{Bi}) and Se (denoted as Cr_{Se}), but also the large defect complexes containing pairs of Cr-atoms, such as the $Cr_{Bi}-Cr_{Se}$ and $Cr_{Bi}-Cr_I$. As illustrated in Figure 4b, the predominant defects in the system were found to be Cr_I^{3+}, Cr_{Bi}^0, and $(Cr_{Bi}-Cr_I)^{3+}$

TABLE 2. Calculated Magnetic Moments of the Low-Energy Cr Related Defects in Bi_2Se_3 and That Derived from XMCD Measurements As Described in the Text[a]

Cr defect	method	ΔH (eV)	m_{spin} (μ_B/atom)	m_{orb} (μ_B/atom)	m_{total} (μ_B/atom)
3%	XMCD		2.05 ± 0.20	-0.05 ± 0.02	2.00 ± 0.20
3%	PBE		1.90	−0.03	1.87
Cr_I^{3+}	PBE	−0.03	2.98	−0.03	2.95
Cr_{Bi}^0	PBE	−0.21	2.93	−0.02	2.91
$(Cr_I-Cr_{Bi})^{3+}$	PBE	−0.68	0.01	−0.04	−0.03

[a] The calculated results include SOC and correspond to the E_F at the CBM with μ_{Cr} and μ_{Bi} equal to their respective bulk values.

complex whose calculated ΔH, excluding SOC, for Fermi energies (E_F) ranging from the valence band maximum (VBM) to the conduction band minimum (CBM) are presented in Figure 4a. We ruled out the possibilities of Cr_{Se} and $Cr_{Se}-Cr_{Bi}$ as the ΔH of them was found to be high (>1 eV). Table 2 presents the ΔH and the magnetic moments of the three low-energy defects, namely, Cr_I, Cr_{Bi}, and $Cr_{Bi}-Cr_I$ calculated including SOC. While both Cr_{Bi} and Cr_I have m_{spin} of $\sim 3\ \mu_B$/atom, the $Cr_{Bi}-Cr_I$ pair is antiferromagnetic (with the high-spin magnetic configuration 75 meV higher in energy) with a nearly vanished m_{spin}. In consistent with the XMCD-derived m_{orb}, the calculation also gives small and negative m_{orb} for the Cr dopants due to the effect of the crystal field. This indicates that Cr retains its small SOC nature, even when incoopertaed into a strong SOC system like Bi_2Se_3.

Figure 5 presents the dependence of the Cr content, average magnetic moment, and the relative concentrations, respectively, of the most common Cr related defects as a function of the chemical potential of Cr with the E_F pinned at the CBM. While the antiferromagnetic $Cr_{Bi}-Cr_I$ pair is the dominant defect for large Cr concentrations, as the Cr chemical potential decreases (and hence the amount of incorporated Cr), entropy works against the pair formation, and Cr_{Bi} becomes the dominant defect. This can be seen in Figure 5b, which shows the relative probabilities of the different defects as a function of m_{Cr} which was calculated by minimizing the free energy of the system with respect to the number of defects (see the Supporting Information). It should be noted that the position of the crossover between the stability of the Cr_{Bi} and $Cr_{Bi}-Cr_I$ defects, depicted in Figure 5b, depends on the m_{Bi}. As we tend toward Se-rich growth conditions, Cr_{Bi} becomes the dominant defect for all Cr concentrations. We treated the m_{Bi} as a fitting parameter and find that the observed data for m_{spin} can be best described when $m_{Bi} \approx 150$ meV below m_{Bi}^{bulk}. This proximity to the Birich condition is well observed in MBE grown samples which typically have high Se vacancy concentrations, despite their high Se deposition rates.[49,50] The dependence of the average magnetic

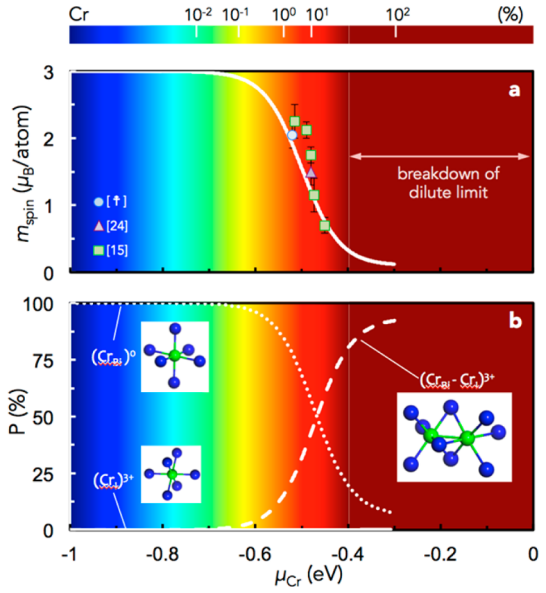

Figure 5. Dependence of (a) m_{spin} and (b) the fraction of the three predominant defects Cr_I^{3+}, Cr_{Bi}^0, and $(Cr_{Bi}-Cr_I)^{3+}$, as a function of the chemical potential of Cr (μ_{Cr}). The zero point of the μ_{Cr} is that of bulk Cr and μ_{Bi} is 150 meV below that of μ_{Bi}^{bulk}. The uppermost scale is an indication of the Cr doping concentration as defined in the text. The brown coloring corresponds to very high defect concentration, in and near where the dilute approximation dramatically fails. The experimentally measured m_{spin} of $Bi_{2-x}Cr_xSe_3$ with varing x have been taken from the literature and gathered in (a) in comparison with the calculation. Dagger symbol (†) refers to this work. Note our definition of the doping concentration differs by a factor of ~2.5 that by Hazzen et al.; hence, the numbers quoted here are larger than that presented in the original paper.[15]

moment per Cr is shown in Figure 5a. The change in stability between Cr_{Bi} and the $Cr_{Bi}-Cr_I$ pair leads to an average magnetic moment which explictly depends on the Cr chemical potential. In agreement with the ponieering reports by Zhang et al.,[17,47] we found that Bi substitutional sites are more stable than interstitial sites for Cr impurities. However, the $Cr_{Bi}-Cr_I$ bonding can significantly alter ΔH, leaving the $(Cr_{Bi}-Cr_I)^{3+}$ complex even lower in energy than either Cr_{Bi} or Cr_I for high Cr doping concentrations. The spontaneous coexistence of ferro- and antiferromagnetic Cr in $Bi_{2-x}Cr_xSe_3$ explains not only the experimental results of our work based on XMCD, but also observations such as by Haazen et al.[48] using SQUID-VSM and by Collins-McIntyre et al.[24] using PNR, who both reported mismatches between the observed magnetic moment of $Bi_{2-x}Cr_xSe_3$ and the Hund's rule value of 3 μ_B/atom for substitutional Cr^{3+} on Bi sites. In consistent with the pioneering experimental reports,[5,49,50] we found that the growth temperature varying between 200 and 300 °C results in no significant difference of the type and distribution the Cr-related defects while below 200 °C, more antiferro-magnetic Cr defects can presence.

CONCLUSIONS

To summarize, we have presented a comprehensive study of the Cr m_{spin} and m_{orb} of a prototype magnetic TI, that is, $Bi_{2-x}Cr_xSe_3$, in the ultrathin limit which is expected to give rise to QAH effect. The high quality $Bi_{1.94}Cr_{0.06}Se_3$/Si(111) epitaxial thin film was prepared using MBE, carefully characterized with STEM, magnetotransport and XMCD measurements. We have quantitatively addressed the m_{spin} and m_{orb} of the $Bi_{2-x}Cr_xSe_3$/Si(111) thin films and the results agree well with DFT caculations. The XMCD-derived m_{spin} is remarkably lower than Hund's rule value and the m_{orb} is negative and largely quecnhed. We obtained a remarkable fraction of the $(Cr_{Bi}-Cr_I)^{3+}$ antiferromagnetic dimers in $Bi_{2-x}Cr_xSe_3$ for $0.02 < x < 0.40$, which has been neglected in previously reported studies. The spontaneous coexistence of ferro- and antiferro-magnetic Cr defects in $Bi_{2-x}Cr_xSe_3$ explains the experimental observations of this work as well as those based on conventional magnetometry that universally report magnetic moments significantly lower than that predicted by the Hund's rule. Our work provides direct evidence for the detailed magnetic states of the magnetically doped TIs in thin film form. Future work to explore the tuning of the magnetization of TIs and its dependence on the band filling will have strong implications for both fundamental physics and emerging spintronics technology.

METHODS

Sample Preparations. The 10 nm $Bi_{2-x}Cr_xSe_3$ thin films used in this study were grown in ultrahigh vacuum (UHV) using a PerkinElmer MBE system on Si(111) substrates using the well-established recipe.[49,50] High-purity Bi (99.9999%) was evaporated from conventional effusion cells at 470 °C, while Se (99.99%) was created from a cracker cell (SVTA) at 240 °C. The substrates were preannealed at 200 °C in UHV until the two-dimensional streak pattern appeared as monitored by the real-time reflection high-energy electron diffraction (RHEED). The desired doping concentrations of Cr were obtained by evaporating Cr (99.99%) from the effusion cell at different temperatures and calibrated by energy dispersive X-ray analysis. Immediately after the growth of the $Bi_{1.94}Cr_{0.06}Se_3$ thin film, 2 nm Al was *in situ* evaporated onto the sample to protect it from oxidation and environmental doping during transport to the synchrotron facility.

ΔH Calculations. The *first-principles* DFT calculations were performed within the Perdew–Burke–Ernzerhof (PBE) generalized gradient approximation (GGA).[51] The Bi (5*d*, 6*s*, 6*p*), Se (4*s*, 4*p*), and Cr (3*p*, 3*d*, 4*s*) orbitals are explicitly treated in the valence and interactions between the ion cores and valence electrons are described by the projector augmented wave (PAW)[52,53] method as implemented in the VASP code.[54,55] Since SOC has shown to be important to describe the defect properties of Bi_2Se_3,[56] the magnetic properties and formation energies of the low energy defects were also calculated with SOC implemented in the all-electron part of the PAW Hamiltonian within the muffin-tin spheres. The basis set consisted of plane waves with a kinetic energy cutoff of 270 eV and the total energy was calculated with a Brillouin zone sampling of

$2 \times 2 \times 2$.[57] Structural relaxations of the defects were performed in a 4×4 supercell containing 3 quintuple layers (QLs) with 95 Bi and 145 Se atoms and proceeded until the largest Hellmann−Feynman force was less than 0.025 eV/A. The ΔH of the defects were calculated in the low-density limit according to

$$\Delta H = E(D^q) - E_{\text{bulk}} + \sum_i \Delta n_i \mu + q(E_F + E_{VBM}) \quad (2)$$

where $E(D^q)$, E_{bulk}, μ_i, and Δn_i, respectively, represent the energy of the supercell containing the defect in charge state q, the energy of the defect-free bulk supercell, the chemical potential of the ith atomic species, and the number of those which has changed in the formation of the defect.[58]

Conflict of Interest: The authors declare no competing financial interest.

Acknowledgment. This work is supported by the State Key Program for Basic Research of China (Grant Nos. 2014CB921101, 2013CB934600, and 2011CB921404), NSFC (Grant Nos. 61274102, 61474061 21473168, 11174244, 51390474, and 11234011), Zhejiang Provincial Natural Science Foundation of China (LR12A04002), the Ministry of Education (20120101110087, IRT13037), and UK STFC. Diamond Light Source is acknowledged for beamtime on I10. D.W. acknowledges support of the Defense Award Research Project Agency (DARPA), Award No. N66001-12-1-4304, and S.B.Z. acknowledges support of the US Department of Energy (DOE) under Grant No. DE-SC0002623. Supercomputer time was provided by NERSC under the Grant No. DE-AC02-05CH11231 and the Center for Computational Innovations (CCI) at Rensselaer Polytechnic Institute.

Supporting Information Available: The Supporting Information is available free of charge on the ACS Publications website at DOI: 10.1021/acsnano.5b03980.

Multiplet calculations and *ab initio* calculations (PDF)

REFERENCES AND NOTES

1. Chang, C.-Z.; Zhang, J.; Feng, X.; Shen, J.; Zhang, Z.; Guo, M.; Li, K.; Ou, Y.; Wei, P.; Wang, L.-L.; et al. Experimental Observation of the Quantum Anomalous Hall Effect in a Magnetic Topological Insulator. *Science* **2013**, *340*, 167–170.
2. Liu, C.-X.; Qi, X.-L.; Dai, X.; Fang, Z.; Zhang, S.-C. Quantum Anomalous Hall Effect in $Hg_{1-y}Mn_yTe$ Quantum Wells. *Phys. Rev. Lett.* **2008**, *101*, 146802.
3. Chen, Y. L.; Chu, J.-H.; Analytis, J. G.; Liu, Z. K.; Igarashi, K.; Kuo, H.-H.; Qi, X. L.; Mo, S. K.; Moore, R. G.; Lu, D. H.; et al. Massive Dirac Fermion on the Surface of a Magnetically Doped Topological Insulator. *Science* **2010**, *329*, 659–662.
4. Qin, W.; Zhang, Z. Persistent Ferromagnetism and Topological Phase Transition at the Interface of a Superconductor and a Topological Insulator. *Phys. Rev. Lett.* **2014**, *113*, 266806.
5. Liu, W.; He, L.; Xu, Y.; Murata, K.; Onbasli, M. C.; Lang, M.; Maltby, N. J.; Li, S.; Wang, X.; Ross, C. a.; et al. Enhancing Magnetic Ordering in Cr-Doped Bi2Se3 Using High-T_C Ferrimagnetic Insulator. *Nano Lett.* **2015**, *15*, 764–769.
6. Tse, W.-K.; MacDonald, a. H. Giant Magneto-Optical Kerr Effect and Universal Faraday Effect in Thin-Film Topological Insulators. *Phys. Rev. Lett.* **2010**, *105*, 057401.
7. Qi, X.; Li, R.; Zang, J.; Zhang, S. Inducing a Magnetic Monopole with Topological Surface States. *Science* **2009**, *323*, 1184–1187.
8. Qi, X.-L.; Hughes, T. L.; Zhang, S.-C. Topological Field Theory of Time-Reversal Invariant Insulators. *Phys. Rev. B: Condens. Matter Mater. Phys.* **2008**, *78*, 195424.
9. Tserkovnyak, Y.; Loss, D. Thin-Film Magnetization Dynamics on the Surface of a Topological Insulator. *Phys. Rev. Lett.* **2012**, *108*, 187201.
10. Dyck, J.; Hájek, P.; Lošt'ák, P.; Uher, C. Diluted Magnetic Semiconductors Based on $Sb_{2-x}V_xTe_3$ ($0.01 \sim x \sim 0.03$). *Phys. Rev. B: Condens. Matter Mater. Phys.* **2002**, *65*, 115212.
11. Dyck, J.; Drašar, Č.; Lošt'ák, P.; Uher, C. Low-Temperature Ferromagnetic Properties of the Diluted Magnetic Semiconductor $Sb_{2-x}Cr_xTe_3$. *Phys. Rev. B: Condens. Matter Mater. Phys.* **2005**, *71*, 115214.
12. Hor, Y. S.; Roushan, P.; Beidenkopf, H.; Seo, J.; Qu, D.; Checkelsky, J. G.; Wray, L. a.; Hsieh, D.; Xia, Y.; Xu, S.-Y.; et al. Development of Ferromagnetism in the Doped Topological Insulator $Bi_{2-x}Mn_xTe_3$. *Phys. Rev. B: Condens. Matter Mater. Phys.* **2010**, *81*, 195203.
13. Kulbachinskii, V. A.; Kaminskii, A.; Yu; Kindo, K.; Narumi, Y.; Suga, K.; Lostak, P.; Svanda, P. Ferromagnetism in New Diluted Magnetic Semiconductor. *Phys. B* **2002**, *311*, 292–297.
14. Chen, Y. L.; Chu, J.-H.; Analytis, J. G.; Liu, Z. K.; Igarashi, K.; Kuo, H.-H.; Qi, X. L.; Mo, S. K.; Moore, R. G.; Lu, D. H.; et al. Massive Dirac Fermion on the Surface of a Magnetically Doped Topological Insulator. *Science* **2010**, *329*, 659–662.
15. Haazen, P. P. J.; Laloë, J.-B.; Nummy, T. J.; Swagten, H. J. M.; Jarillo-Herrero, P.; Heiman, D.; Moodera, J. S. Ferromagnetism in Thin-Film Cr-Doped Topological Insulator Bi_2Se_3. *Appl. Phys. Lett.* **2012**, *100*, 082404.
16. Choi, Y. H.; Jo, N. H.; Lee, K. J.; Yoon, J. B.; You, C. Y.; Jung, M. H. Transport and Magnetic Properties of Cr-, Fe-, Cu-Doped Topological Insulators. *J. Appl. Phys.* **2011**, *109*, 07E312.
17. Zhang, J.-M.; Zhu, W.; Zhang, Y.; Xiao, D.; Yao, Y. Tailoring Magnetic Doping in the Topological Insulator Bi_2Se_3. *Phys. Rev. Lett.* **2012**, *109*, 266405.
18. Song, Y. R.; Yang, F.; Yao, M.-Y.; Zhu, F.; Miao, L.; Xu, J.-P.; Wang, M.-X.; Li, H.; Yao, X.; Ji, F.; et al. Large Magnetic Moment of Gadolinium Substituted Topological Insulator: $Bi_{1.98}Gd_{0.02}Se_3$. *Appl. Phys. Lett.* **2012**, *100*, 242403.
19. Chen, T.; Liu, W.; Zheng, F.; Gao, M.; Pan, X.; van der Laan, G.; Wang, X.; Zhang, Q.; Song, F.; Wang, B.; et al. High-Mobility Sm-Doped Bi_2Se_3 Ferromagnetic Topological Insulators and Robust Exchange Coupling. *Adv. Mater.* **2015**, *27*, 4823.
20. Harrison, S. E.; Collins-McIntyre, L. J.; Zhang, S.-L.; Baker, A. A.; Figueroa, A. I.; Kellock, A. J.; Pushp, A.; Parkin, S. S. P.; Harris, J. S.; van der Laan, G.; et al. Study of Dy-Doped Bi_2Te_3: Thin Film Growth and Magnetic Properties. *J. Phys.: Condens. Matter* **2015**, *27*, 245602.
21. Figueroa, A. I.; van der Laan, G.; Collins-McIntyre, L. J.; Zhang, S.-L.; Baker, a. a.; Harrison, S. E.; Schönherr, P.; Cibin, G.; Hesjedal, T. Magnetic Cr Doping of Bi_2Se_3: Evidence for Divalent Cr from X-Ray Spectroscopy. *Phys. Rev. B: Condens. Matter Mater. Phys.* **2014**, *90*, 134402.
22. Collins-McIntyre, L. J.; Watson, M. D.; Baker, A. A.; Zhang, S. L.; Coldea, A. I.; Harrison, S. E.; Pushp, A.; Kellock, A. J.; Parkin, S. S. P.; van der Laan, G.; et al. X-Ray Magnetic Spectroscopy of MBE-Grown Mn-Doped Bi_2Se_3 Thin Films. *AIP Adv.* **2014**, *4*, 127136.
23. Watson, M. D.; Collins-McIntyre, L. J.; Shelford, L. R.; Coldea, a I.; Prabhakaran, D.; Speller, S. C.; Mousavi, T.; Grovenor, C. R. M.; Salman, Z.; Giblin, S. R.; et al. Study of the Structural, Electric and Magnetic Properties of Mn-Doped Bi_2Te_3 Single Crystals. *New J. Phys.* **2013**, *15*, 103016.
24. Watson, M. D.; Collins-McIntyre, L. J.; Shelford, L. R.; Coldea, a I.; Prabhakaran, D.; Speller, S. C.; Mousavi, T.; Grovenor, C. R. M.; Salman, Z.; Giblin, S. R.; et al. Study of the Structural, Electric and Magnetic Properties of Mn-Doped Bi_2Te_3 Single Crystals. *New J. Phys.* **2013**, *15*, 103016.
25. Edmonds, K. W.; van der Laan, G.; Farley, N. R. S.; Campion, R. P.; Gallagher, B. L.; Foxon, C. T.; Cowie, B. C. C.; Warren, S.; Johal, T. K. Magnetic Linear Dichroism in the Angular Dependence of Core-Level Photoemission from (Ga,Mn) As Using Hard X Rays. *Phys. Rev. Lett.* **2011**, *107*, 197601.
26. Ruderman, M. A.; Kittel, C. Indirect Exchange Coupling of Nuclear Magnetic Moments by Conduction Electrons. *Phys. Rev.* **1954**, *96*, 99–102.
27. Yosida, K. Magnetic Properties of Cu-Mn Alloys. *Phys. Rev.* **1957**, *106*, 893–898.
28. Jungwirth, T.; Sinova, J.; Masek, J.; Kucera, J.; MacDonald, A. H. Rev. Theory Of Ferromagnetic (III,Mn)V Semiconductors. *Rev. Mod. Phys.* **2006**, *78*, 809–864.
29. Hong, N. H.; Sakai, J.; Poirot, N.; Brizé, V. Room-Temperature Ferromagnetism Observed in Undoped Semiconducting And Insulating Oxide Thin Films. *Phys. Rev. B: Condens. Matter Mater. Phys.* **2006**, *73*, 132404.

30. Checkelsky, J. G.; Ye, J.; Onose, Y.; Iwasa, Y.; Tokura, Y. Dirac-Fermion-Mediated Ferromagnetism in a Topological Insulator. *Nat. Phys.* **2012**, *8*, 729–733.
31. Chang, C.-Z.; et al. Thin Films of Magnetically Doped Topological Insulator with Carrier-Independent Long-Range Ferromagnetic Order. *Adv. Mater.* **2013**, *25*, 1065–1070.
32. Tjeng, L. H.; Idzerda, Y. U.; Rudolf, P.; Sette, F.; Chen, C. T. Soft-X-Ray Magnetic Circular Dichroism: A New Technique for Probing Magnetic Properties of Magnetic Surfaces and Ultrathin Films. *J. Magn. Magn. Mater.* **1992**, *109*, 288–292.
33. Kronast, F.; Ovsyannikov, R.; Vollmer, A.; Dürr, H. A.; Eberhardt, W.; Imperia, P.; Schmitz, D.; Schott, G. M.; Ruester, C.; Gould, C.; et al. Mn 3*d* electronic configurations in $(Ga_{1-x}Mn_x)As$ ferromagnetic semiconductors and their influence on magnetic ordering. *Phys. Rev. B: Condens. Matter Mater. Phys.* **2006**, *74*, 235213.
34. Liu, W. Q.; Wang, W. Y.; Wang, J. J.; Wang, F. Q.; Lu, C.; Jin, F.; Zhang, a.; Zhang, Q. M.; van der Laan, G.; Xu, Y. B.; et al. Atomic-Scale Interfacial Magnetism in Fe/Graphene Heterojunction. *Sci. Rep.* **2015**, *5*, 11911.
35. Vobornik, I.; Manju, U.; Fujii, J.; Borgatti, F.; Torelli, P.; Krizmancic, D.; Hor, Y. S.; Cava, R. J.; Panaccione, G. Magnetic Proximity Effect as a Pathway to Spintronic Applications of Topological Insulators. *Nano Lett.* **2011**, *11*, 4079–4082.
36. Li, J.; Wang, Z. Y.; Tan, A.; Glans, P.-A.; Arenholz, E.; Hwang, C.; Shi, J.; Qiu, Z. Q. Magnetic Dead Layer at the Interface between a Co Film and the Topological Insulator Bi_2Se_3. *Phys. Rev. B: Condens. Matter Mater. Phys.* **2012**, *86*, 054430.
37. Tserkovnyak, Y.; Pesin, D. A.; Loss, D. Spin and orbital magnetic response on the surface of a topological insulator. *Phys. Rev. B: Condens. Matter Mater. Phys.* **2015**, *91*, 041121.
38. Clarke, S. M.; Freedman, D. E. $(BiSe)_{1.23}CrSe_2$ and $(BiSe)_{1.22}(Cr_{1.2}Se_2)_2$: First Structurally Characterized Bi-Se-Cr Ternary Compounds. *Inorg. Chem.* **2015**, *54*, 2765.
39. Ji, H.; Allred, J. M.; Ni, N.; Tao, J.; Neupane, M.; Wray, a.; Xu, S.; Hasan, M. Z.; Cava, R. J. Bulk Intergrowth of a Topological Insulator with a Room-Temperature Ferromagnet. *Phys. Rev. B: Condens. Matter Mater. Phys.* **2012**, *85*, 165313.
40. Nagaosa, N.; Sinova, J.; Onoda, S.; MacDonald, A. H.; Ong, N. P. Anomalous Hall effect. *Rev. Mod. Phys.* **2010**, *82*, 1539–1592.
41. Wang, H.; Bencok, P.; Steadman, P.; Longhi, E.; Zhu, J.; Wang, Z. Complete Polarization Analysis of an APPLE II Undulator Using a Soft X-Ray Polarimeter. *J. Synchrotron Radiat.* **2012**, *19*, 944–948.
42. Thole, B.; Carra, P.; Sette, F.; van der Laan, G. X-Ray Circular Dichroism as a Probe of Orbital Magnetization. *Phys. Rev. Lett.* **1992**, *68*, 1943–1946.
43. Carra, P.; Thole, B. T.; Altarelli, M.; Wang, X. X-Ray Circular Dichroism and Local Magnetic Fields. *Phys. Rev. Lett.* **1993**, *70*, 694–697.
44. Liu, W. Q.; Xu, Y. B.; Wong, P. K. J.; Maltby, N. J.; Li, S. P.; Wang, X. F.; Du, J.; You, B.; Wu, J.; Bencok, P.; et al. Spin and Orbital Moments of Nanoscale Fe_3O_4 Epitaxial Thin Film on MgO/GaAs(100). *Appl. Phys. Lett.* **2014**, *104*, 142407.
45. Liu, W. Q.; Song, M. Y.; Maltby, N. J.; Li, S. P.; Lin, J. G.; Samant, M. G.; Parkin, S. S. P.; Bencok, P.; Steadman, P.; Dobrynin, A.; et al. X-Ray Magnetic Circular Dichroism Study of Epitaxial Magnetite Ultrathin Film on MgO(100). *J. Appl. Phys.* **2015**, *117*, 17E121.
46. van der Laan, G.; Thole, B. T. Strong Magnetic X-Ray Dichroism in 2*p* Absorption Spectra of 3*d* Transition-Metal Ions. *Phys. Rev. B: Condens. Matter Mater. Phys.* **1991**, *43*, 13401.
47. Zhang, J.-M.; Ming, W.; Huang, Z.; Liu, G.-B.; Kou, X.; Fan, Y.; Wang, K. L.; Yao, Y. Stability, electronic, and magnetic properties of the magnetically doped topological insulators Bi_2Se_3, Bi_2Te_3 and Sb_2Te_3. *Phys. Rev. B: Condens. Matter Mater. Phys.* **2013**, *88*, 235131.
48. Zhang, D.; Richardella, A.; Rench, D. W.; Xu, S.-Y.; Kandala, A.; Flanagan, T. C.; Beidenkopf, H.; Yeats, A. L.; Buckley, B. B.; Klimov, P. V.; et al. Interplay between Ferromagnetism, Surface States, and Quantum Corrections in a Magnetically Doped Topological Insulator. *Phys. Rev. B: Condens. Matter Mater. Phys.* **2012**, *86*, 205127.
49. Kou, X. F.; Jiang, W. J.; Lang, M. R.; Xiu, F. X.; He, L.; Wang, Y.; Yu, X. X.; Fedorov, A. V.; Zhang, P.; Wang, K. L. Magnetically Doped Semiconducting Topological Insulators. *J. Appl. Phys.* **2012**, *112*, 063912.
50. Kou, X.; He, L.; Lang, M.; Fan, Y.; Wong, K.; Jiang, Y.; Nie, T.; Jiang, W.; Upadhyaya, P.; Xing, Z.; et al. Manipulating Surface-Related Ferromagnetism in Modulation-Doped Topological Insulators. *Nano Lett.* **2013**, *13*, 4587–4593.
51. Perdew, J. P.; Burke, K.; Ernzerhof, M. Generalized Gradient Approximation Made Simple. *Phys. Rev. Lett.* **1996**, *77*, 3865.
52. Blochl, P. E. Projector Augmented-Wave Method. *Phys. Rev. B: Condens. Matter Mater. Phys.* **1994**, *50*, 17953.
53. Kresse, G.; Joubert, D. From Ultrasoft Pseudopotentials to the Projector Augmented-Wave Method. *Phys. Rev. B: Condens. Matter Mater. Phys.* **1999**, *59*, 1758–1775.
54. Kresse, G.; Hafner, J. *Ab initio* Molecular Dynamics for Liquid Metals. *Phys. Rev. B: Condens. Matter Mater. Phys.* **1993**, *47*, 558.
55. Kresse, G.; Furthmüller, J. Efficient Iterative Schemes for *Ab initio* Total-Energy Calculations Using a Plane-Wave Basis Set. *Phys. Rev. B: Condens. Matter Mater. Phys.* **1996**, *54*, 11169–11186.
56. West, D.; Sun, Y. Y.; Zhang, S. B.; Zhang, T.; Ma, X.; Cheng, P.; Zhang, Y. Y.; Chen, X.; Jia, J. F.; Xue, Q. K. Identification of Magnetic Dopants on the Surfaces of Topological Insulators: Experiment and Theory for Fe on Bi_2Te_3(111). *Phys. Rev. B: Condens. Matter Mater. Phys.* **2012**, *85*, 081305.
57. Monkhorst, H. J.; Pack, J. D. Special Points for Brillouin-Zone Integrations. *Phys. Rev. B* **1976**, *13*, 5188.
58. Zhang, S.; Northrup, J. Chemical Potential Dependence of Defect Formation Energies in GaAs: Application to Ga Self-Diffusion. *Phys. Rev. Lett.* **1991**, *67*, 2339–2342.